

Article

# Tropical Cyclone-Induced Sea Surface Temperature Responses in the Northern Indian Ocean

Jianmin Yu <sup>1,†</sup> , Haibin Lv <sup>2,†</sup>, Simei Tan <sup>1,2</sup> and Yuntao Wang <sup>1,\*</sup> 

<sup>1</sup> State Key Laboratory of Satellite Ocean Environment Dynamics, Second Institute of Oceanography, Ministry of Natural Resources, Hangzhou 310012, China

<sup>2</sup> Jiangsu Key Laboratory of Marine Bioresources and Environment/Jiangsu Key Laboratory of Marine Biotechnology, Jiangsu Ocean University, Lianyungang 222069, China

\* Correspondence: yuntao.wang@sio.org.cn; Tel.: +86-571-81963629

† These authors contributed equally to this work.

**Abstract:** Tropical cyclones (TCs) exert a significant influence on the upper ocean, leading to sea surface temperature (SST) changes on a global scale. However, TC-induced SST responses exhibit considerable variability in the northern Indian Ocean (NIO), and the general understanding of these responses remains limited. This paper investigates the SST changes caused by 96 TCs over an 18-year period in the NIO. Through a composite analysis utilizing satellite SST data, a comprehensive study is conducted to examine the relationship between TC characteristics, including wind speed and translation speed, and the associated SST changes. The overall findings reveal that within a radius of 300 km from the TC center, SST decreases were observed at 1702 (86%) locations, with an average SST response to TC of  $-0.46$  °C and a maximum decrease of  $-2.07$  °C. The most significant reduction in SST typically occurred two days after the passage of TCs, followed by a gradual recovery period exceeding 15 days for the SSTs to return to their initial values. Consistent with findings in other ocean basins, stronger and slower-moving TCs induced more substantial cooling effects. Conversely, at 279 (14%) locations, particularly associated with TCs of weaker intensities, SST increases were observed following the TC passage. Notably, 140 of these locations were situated at low latitudes, specifically between 8° N and 15° N. This study provides a quantitative analysis of the comprehensive SST response to TCs in the NIO.

**Keywords:** tropical cyclone; sea surface temperature; northern Indian Ocean; oceanic responses



**Citation:** Yu, J.; Lv, H.; Tan, S.; Wang, Y. Tropical Cyclone-Induced Sea Surface Temperature Responses in the Northern Indian Ocean. *J. Mar. Sci. Eng.* **2023**, *11*, 2196. <https://doi.org/10.3390/jmse11112196>

Academic Editors: Chunyan Li, Mohammad Nabi Allahdadi and João Miguel Dias

Received: 30 September 2023

Revised: 27 October 2023

Accepted: 7 November 2023

Published: 18 November 2023



**Copyright:** © 2023 by the authors. Licensee MDPI, Basel, Switzerland. This article is an open access article distributed under the terms and conditions of the Creative Commons Attribution (CC BY) license (<https://creativecommons.org/licenses/by/4.0/>).

## 1. Introduction

A tropical cyclone (TC) is an intensive weather system that forms over the tropical or subtropical ocean surface [1]. These natural phenomena are among the most destructive events on Earth, characterized by powerful winds [2], extensive storm surges [3], and heavy rainfall, leading to prolonged precipitation [4] and causing severe damage to coastal communities [5].

The formation of a TC relies on specific thermodynamic conditions, including warm sea surface temperatures (SSTs) exceeding 26.5 °C, the presence of moist air rising from near the ocean surface, and unstable atmospheric conditions [6]. Additionally, a favorable environment requires weak vertical wind shear in the lower atmosphere and the presence of the Coriolis force [7]. Consequently, TCs predominantly occur at low latitudes, but they avoid the equatorial regions [8].

The north Indian Ocean (NIO) accounts for 13% of the total annual TCs worldwide [9]. Unfortunately, due to densely populated areas and limited infrastructure for disaster mitigation, more than 80% of global TC-related deaths occur in the NIO [10,11]. For example, TC Nargis impacted approximately 1.5 million people in Myanmar and resulted in over 130,000 deaths [12]. Recent observations indicate that TCs in the NIO are intensifying at an alarming rate due to climate change [13] and are moving closer to coastal regions [14].

TCs extract a substantial influx of heat from the ocean via sensible and latent heat fluxes, enabling TCs to sustain and potentially intensify [15]. For example, TC Phailin, which formed in the Arabian Sea, rapidly intensified from a cyclone storm to a severe TC within a span of just 24 h [16]. Furthermore, Deshpande et al. [17] found an increase in both the frequency and intensity of TCs in the NIO from 1980 to 2019. Understanding the dynamic processes of TCs and accurately predicting their areas of impact are becoming increasingly crucial for effective disaster prevention [18].

The prediction of TC impacts relies on a comprehensive understanding of their genesis and development. As TCs involve strong interactions between the atmosphere and the ocean, their intensity and trajectories are significantly influenced by the underlying oceanic conditions, such as surface cooling [19]. TCs cool the ocean along their path and in their vicinity through various processes, including Ekman pumping, which results from large-scale flow divergence from the TC center, and vertical mixing induced by powerful winds [8,20–22]. Observations and analysis of TC Chapala, for example, revealed that the initial cooling of SSTs was primarily attributed to enhanced evaporation caused by strong winds [23]. Subsequently, mixing and upwelling led to the redistribution of water throughout the upper ocean or the upwelling of subsurface water to the surface, resulting in significant cooling [23]. Multiple TC cases provide observational evidence of local cooling exceeding 3 °C [24–27], although the degree of TC-induced cooling can vary significantly, with super TC Odisha inducing cooling of up to 6 °C [28].

TC-induced SST cooling is closely linked to TC characteristics, specifically intensity and translational speed [29,30]. During the initial stage of a TC, when a tropical disturbance manifests as a significant change in wind speed [31], cooling effects are negligible. The life cycle of a TC typically ranges from 3 to 8 days, with a maximum duration of 20 days and a minimum of 1 to 2 days [1]. Greater cooling values are associated with more intense TCs, particularly those with slower translation speeds [32–34]. Strong TCs can generate powerful near-inertial internal waves and turbulence that penetrate to depths of 100–200 m in the ocean, resulting in a remarkable decrease in SST [35,36]. Slow-moving TCs have a longer duration to induce mixing and upwelling over the upper ocean, leading to a deeper mixed layer and a larger SST anomaly ( $\delta$ SST) [37]. Notably, TC Nilofar, characterized by a slow translation speed of 0.9–1.3 m/s, exhibited extraordinary cooling of 5 °C [38].

Previous studies on TC–ocean interactions have predominantly focused on the North-west Pacific Ocean and the Atlantic Ocean [39]. Limited research has provided a general description of TCs in the NIO, including their seasonal patterns and the factors influencing TC-induced oceanic responses [40,41]. Moreover, analysis of TCs in the NIO have primarily been based on individual cases [42,43], with a focus on TCs that had significant impacts on the upper ocean. Although we possess a fundamental understanding of the response of upper ocean parameters to TCs in the global ocean, numerous observations contradict expectations due to the complex nature of ocean characteristics and variations among individual TCs [44]. This article presents a comprehensive analysis of all TCs in the NIO over the past 18 years to develop a quantitative understanding of TC-induced cooling. The study further investigates the underlying mechanisms that determine oceanic responses based on TC features and ocean conditions. Unusual cases of oceanic responses, such as SST warming, are also identified to comprehend their temporal and spatial patterns. The findings of this study contribute to a general understanding of TC-induced SST changes in the NIO and enhance future prediction of TC impacts.

## 2. Materials and Methods

### 2.1. Dataset of Tropical Cyclones

The dataset for TCs consists of track data obtained from the Joint Typhoon Warning Center (JTWC), which includes information such as the center location (longitude and latitude), time, and maximum sustained surface wind data. The study covers a time span of 18 years, specifically from 1 January 2003 to 31 December 2020. The TC data obtained from the JTWC are considered the most reliable for this study, as they contain comprehensive

information on TCs in the NIO, particularly in the Arabian Sea 8. The dataset encompasses the spatial range of the NIO, which extends from 0° N to 30° N and from 45° E to 105° E.

To assess the intensity of each TC along its track at 6 h intervals, the data include categorization into one of seven categories (Table 1). The classification is based on the maximum sustained surface wind speed (MSW) near the bottom center of the TC, following the classification system provided by the Indian Meteorological Department (IMD) (<http://www.imd.gov.in/>, accessed on 1 September 2022) [45]. Additionally, the translation speed of each TC is calculated by dividing the distance between the center points of adjacent TCs by the time interval between them.

**Table 1.** Classification of TCs over the NIO.

Category	IMD Intensity Scale	MSW (m/s)
1	Depression (D)	MSW < 14
2	Deep depression (DD)	14 ≤ MSW < 17
3	Cyclone storm (CS)	17 ≤ MSW < 24
4	Severe cyclone storm (SCS)	24 ≤ MSW < 32
5	Very severe cyclone storm (VSCS)	32 ≤ MSW < 46
6	Extremely strong cyclone storm (ESCS)	46 ≤ MSW < 61
7	Super cyclone (SC)	MSW ≥ 61

The daily sea surface temperature (SST) dataset is compiled by merging satellite observations obtained from the MW\_IR of Remote Sensing System (<https://remss.com/>, accessed on 1 April 2023) from 1 January 2003 to 31 December 2020. These observations have a spatial resolution of approximately 9 km. The SST dataset covers the same time span, and the daily climatology is calculated by averaging SST over 18 years for the corresponding date [34]. The incorporate topographic information of the NIO, the 2 arc-minute global relief model of Earth's Topography and ocean bathymetry (ETOPO2) is utilized to derive the necessary data. In order to determine the pre-storm mixed layer depth (MLD), the monthly climatological profile of temperature is obtained from the gridded BOA-ARGO datasets, which have a spatial resolution of 1° [46].

## 2.2. Composite Methods

During the study period, a total of 96 TCs were identified in the NIO. This corresponds to 2250 TC locations recorded at 6 h intervals. Among these locations, 1981 are situated over the ocean and were considered for analysis in this study. The lifespan of a TC is defined from its initial identification until its termination. To capture the temporal evolution of the TCs, a linear interpolation is employed, ranging from 0 to 1 throughout the duration. For each TC location, the SST within a 300 km radius is used for composite analysis, following established methodologies [34]. Specifically, SSTs are considered for a period of 15 days before and after the arrival of the TC. The  $\delta$ SST is calculated at the pixel level by subtracting the corresponding climatological average at each position on the given date. Furthermore, the  $\Delta$ SST is determined for each location by computing the disparity between the averaged  $\delta$ SST over the 15 days following the TC's arrival and the averaged  $\delta$ SST over the 15 days preceding its arrival.

## 3. Results

### 3.1. General TC Features in the NIO

The spatial distribution of the climatologically averaged SST in the NIO reveals notable variations in both zonal and meridional directions (Figure 1a). Lower SSTs, such as 26 °C or lower, are predominantly observed in the western section, around the Arabian Peninsula and off the Somali Peninsula. These areas correspond to the wind-driven upwelling zone [47]. The difference in SST is more pronounced in the Arabian Sea compared to the Bay of Bengal, where SST generally decreases with latitude. Offshore ocean regions, specifically between 0°–18° N and 60°–94° E, typically exhibit average SST values ranging

from 28 °C to 30 °C. The region around Sumatra Island experiences the highest SSTs, reaching approximately 30 °C.

The track of the 96 TCs (Figure 1b) indicate that the majority of TC locations in the entire Bay of Bengal basin and the eastern section of the Arabian Sea are characterized by weaker intensities, typically falling under category 4 or lower. Stronger TCs, classified as category 5 or stronger, are primarily observed in the western section of the Arabian Sea and along the coastal area of the Bay of Bengal. The frequency of TC occurrence in the Arabian Sea is lower compared to the Bay of Bengal. The highest density of TCs is concentrated between 8° N and 20° N, particularly on the western side of the Bay of Bengal. The climatological characteristics of the Arabian Sea and Bay of Bengal, including oceanic and atmospheric environments, play a significant role in TC genesis within each sub-basins [48]. Vertical wind shear and relative humidity in the low- and middle-level troposphere are two major contributing factors that determine TC genesis, with their relative importance varying between the Arabian Sea and Bay of Bengal. This leads to variations in TC occurrences in each region. Some TCs make landfall on the Indian Peninsula, resulting in significant weakening of their intensity, while only a few of them cross land and regain strength as they continue their propagation in the Arabian Sea. The average bathymetry in the Arabian Sea is relatively deep, approximately 2491 m, while the Bay of Bengal has a shallower average depth of 1291 m.

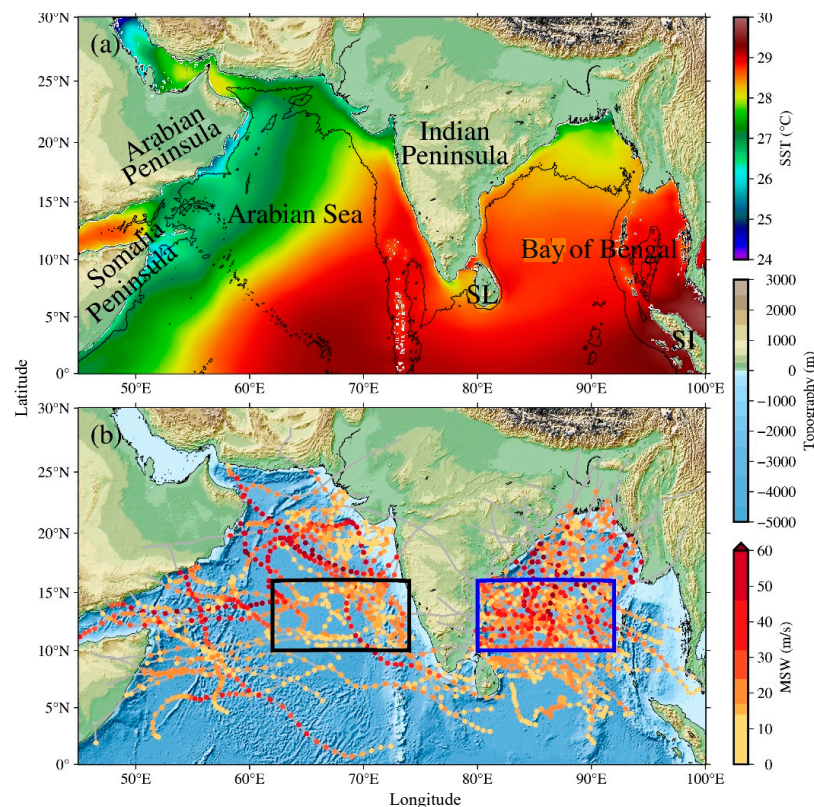


**Figure 1.** (a) Averaged SST in the NIO along with 2500 m isobath (SL: Sri Lanka; SI: Sumatra Island); (b) TC tracks in the NIO overlaid on topography. The color of the TC points indicates the intensity category based on Table 1. The black and blue boxes delineate the highest densities of TCs in the Arabian Sea (10°–16° N and 62°–74° E) and Bay of Bengal (10°–16° N and 80°–92° E), respectively.

The monthly averaged SSTs within the regions with the highest densities of TCs in the Bay of Bengal and the Arabian Sea, as indicated by the boxes in Figure 1b, exhibit distinct seasonal cycles with a weak semiannual cycle (Figure 2a). SST peaks are generally observed in early spring, particularly in May, while a secondary peak occurs in fall, typically in November. In the Arabian Sea, the SST reaches its highest value in May, around 30.3 °C,

and its minimum in August, around 26.8 °C. This pattern closely aligns with the SST variation in the Bay of Bengal, where the highest SST, approximately 30.2 °C, is recorded in May, and the lowest, around 27.3 °C, is observed in January. A notable seasonal variation in TC occurrence is also evident. Spring (March–May), summer (June–August), autumn (September–November), and winter (December–February) account for 18.3%, 10.2%, 53.5%, and 18.0% of the annual TC count, respectively (Figure 2b). Particularly, November experiences over 28.0% of the TC occurrences. In contrast, no TCs were recorded in February, March, or August over the 18-year period examined. Most TCs fall into category 1 and category 3 storms, while intense TCs primarily occur in May, October, and November. Consequently, a higher frequency of strong-intensity TCs is observed during autumn/winter and late spring/early summer in the NIO.

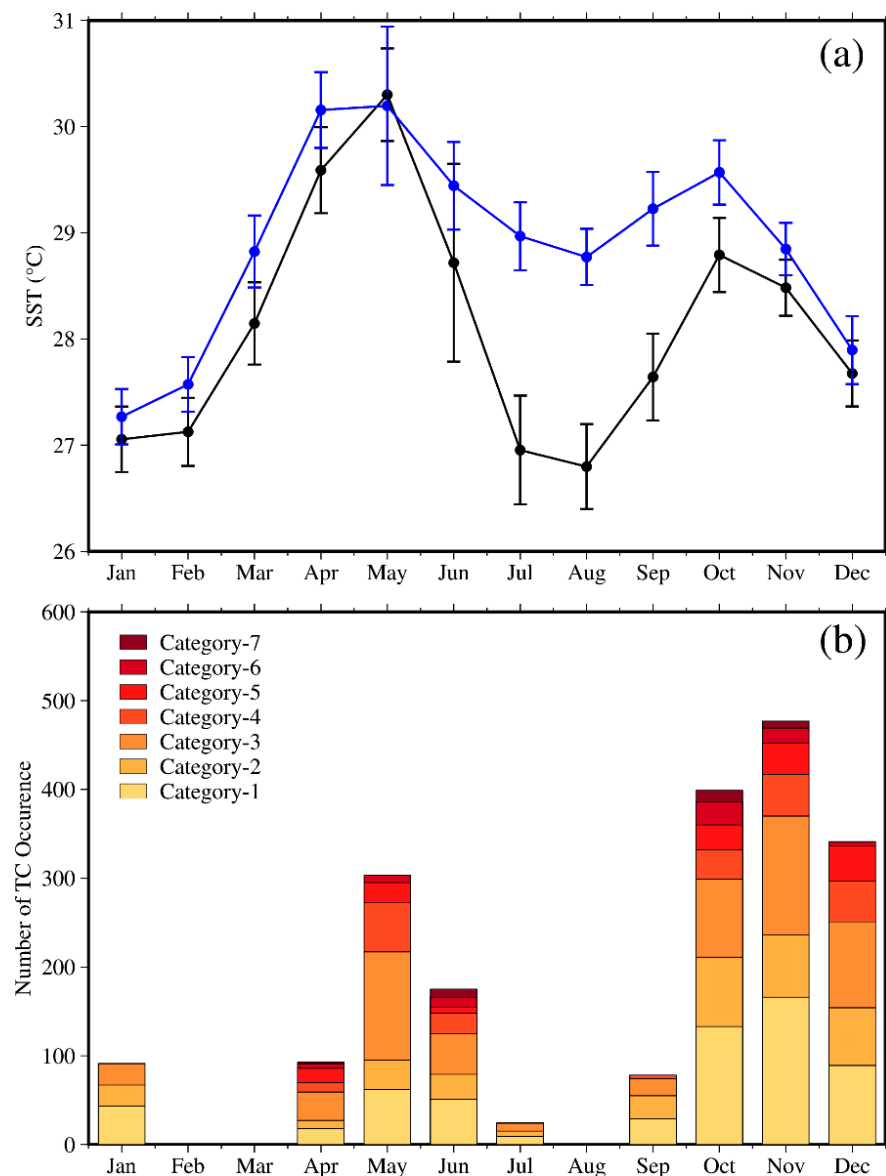


**Figure 2.** (a) Monthly averaged SST and associated standard deviation in the Arabian Sea (black curve) and the Bay of Bengal (blue curve). (b) Monthly number of TC occurrences categorized by different intensity levels.

The wind speed of TCs generally increases during the early and middle phases of their lifespan, meanwhile maintains a relatively stable translation speed (Figure 3a). To analyze this, the lifespan of TCs was divided into 10 groups from the beginning to the end, and the average wind speed and translation speed were calculated within each group. The average wind speed reaches its maximum value, 29.7 m/s, immediately after the middle of a TC’s lifespan. After this peak, the wind speed rapidly decreases. This rapid decrease may be attributed to the fading of TCs as they make landfall, resulting in a short decaying phase. Simultaneously, the translation speed of TCs rapidly increases from 3.2 m/s to 5.0 m/s. Thus, TCs with faster translation speeds are typically associated with lower wind speeds. On the other hand, slow-moving TCs can exhibit high or low wind speeds. This suggests that the relationship between translation speed and wind speed is not straightforward, and other factors may influence the wind speed of TCs. Figure 3b represents a scatterplot of wind speed and translation speed corresponding to the positions of TCs. The wind speed values are predominately within the range of 10–30 m/s, accounting for 73% of the data. Meanwhile, the corresponding translation speeds are concentrated between 0 m/s and 6 m/s.

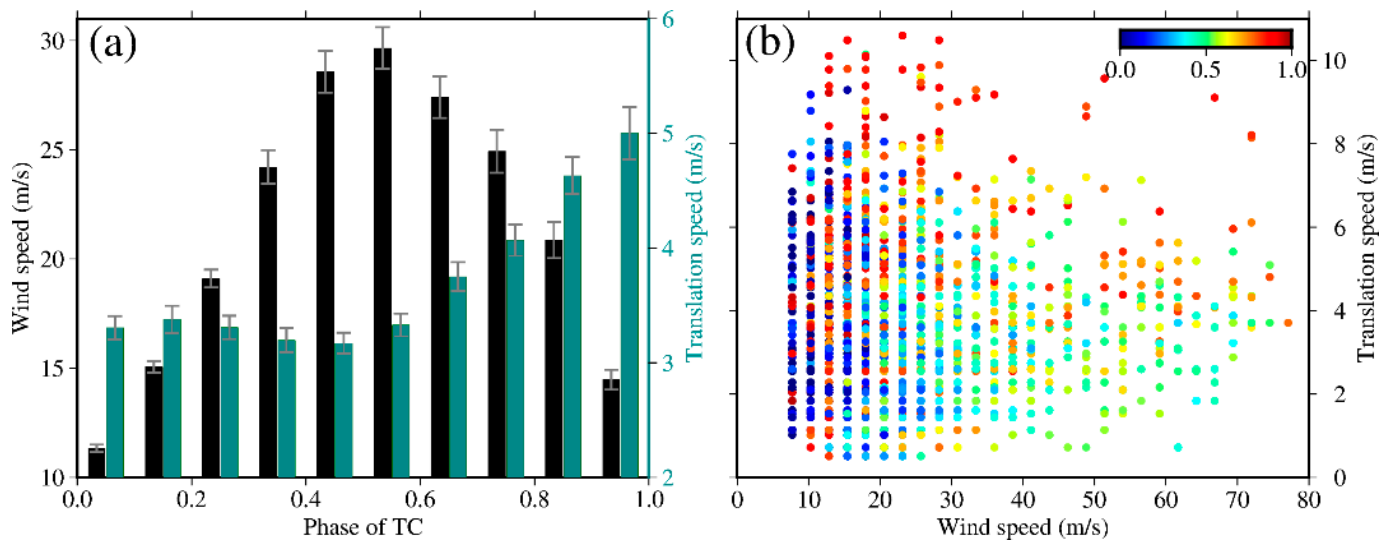


**Figure 3.** The averaged wind speed (black bars) and translation speed (dark green bars) during different phases of TCs with (a) the average (bar) and standard deviation (vertical lines) during different phases of TCs. The phases are denoted by numbers, with 0 representing the beginning and 1 representing the end of a TC. The lifespan of TCs is divided into ten groups, and within each group, the average wind speed and translation speed are calculated. (b) Scatterplot of wind speed and translation speed for all TC locations. The color of the dots indicates the phases of the TCs.

The spatial distribution of areas affected by TCs is depicted by the cumulative duration that a location remains within a 300 km radius of a TC position (Figure 4). This representation aligns well with the TC tracks presented in Figure 1b. Significantly, there are noticeable spatial variations, with the highest concentration of TCs observed in the western section of the Bay of Bengal, specifically between 8° N and 20° N. In this region, the maximum value reaches 245, corresponding to the densest TC tracks. Conversely, the Arabian Sea exhibits a region with the largest number of TCs, totaling 137, and this area tends to have higher-density locations along the eastern section, adjacent to the coast of the Indian Peninsula.

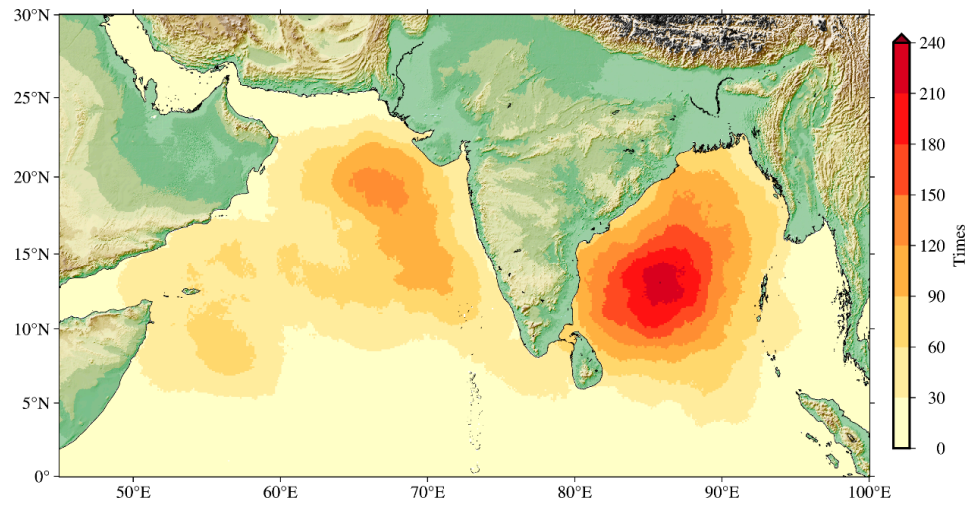


**Figure 4.** Spatial distribution of the frequency of areas impacted by TCs.

### 3.2. Impact of TC on SSTs

The influence of TCs on the ocean can be analyzed by examining the time series of  $\delta$ SST at each TC position (Figure 5). To distinguish the impact of TC-induced changes, the corresponding  $\Delta$ SST was used to sort the results from the largest cooling to the largest warming. The analysis revealed that a majority of locations, specifically 1702 (86%), experienced cooling effects, resulting in a decrease in SST. The maximum cooling observed was more than  $-2.07\text{ }^{\circ}\text{C}$ , indicating substantial cooling in some areas. While less common, warming effects were observed in 279 locations, with the largest increase in SST recorded at  $0.58\text{ }^{\circ}\text{C}$ . It is important to consider that the data used in this analysis were derived from satellite observations, which may introduce some smoothing of minimum values due to cloud coverage, particularly during TC passage. Additionally, it is worth noting that warm anomalies were frequently observed prior to the passage of TCs. Furthermore, it is important to mention that when comparing the merged dataset to individual infrared instruments, the maximum cooling values appeared slightly smaller in the merged dataset.

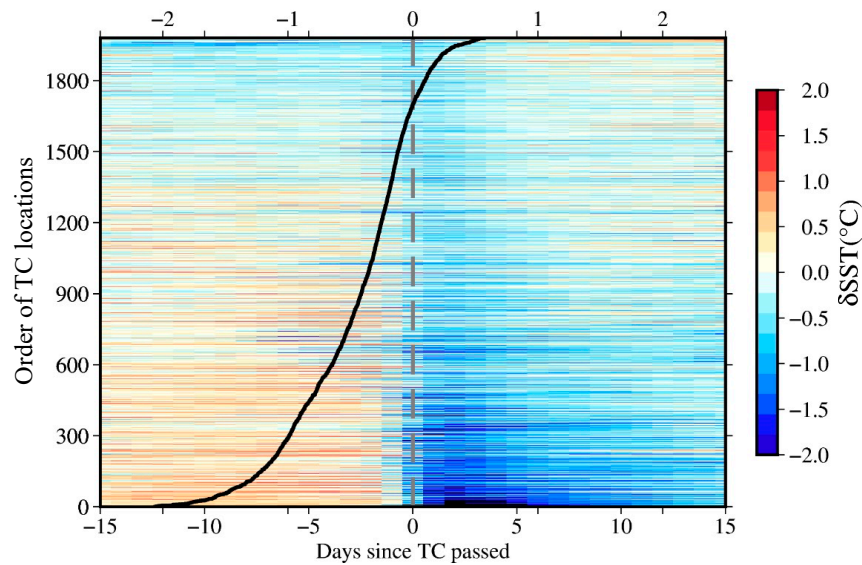


**Figure 5.** Time series of the  $\delta$ SST (shading) for different TC locations. The locations are arranged in descending order based on the magnitude of TC-induced  $\Delta$ SST; corresponding  $\Delta$ SST is depicted by the black curve. The gray dashed line indicates the passage of the TC.

Among the TC locations exhibiting positive  $\Delta$ SST values, 140 points lie within the range of  $8^{\circ}$ – $15^{\circ}$  N, constituting approximately 50.2% of the total number (Figure 6a). Analysis of the corresponding TC tracks reveals a consistent pattern of warming occurring as the TCs move offshore or approach the coast. Many of these tracks also exhibit a tendency for zonal propagation. In terms of temporal distribution, the majority of positive  $\Delta$ SST instances are observed during late autumn/winter. Specifically, 177 cases (63.4%) occurred in November and December when TC frequency is higher, and SST values reach their peak during winter (Figure 2a). Lower wind speeds are conducive to the occurrence of positive  $\Delta$ SST (Figure 6b), with approximately 92.8% of instances recording wind speeds below 25 m/s. The pre-storm SST values corresponding to these cases display significant variability, ranging from a minimum of  $25.9^{\circ}\text{C}$  to a maximum of  $29.5^{\circ}\text{C}$ . When considering other TC center points, approximately 84% of the associated wind speeds fall within the range of 10 m/s to 40 m/s, while the corresponding SST values concentrate between  $25.9^{\circ}\text{C}$  and  $31.4^{\circ}\text{C}$  (Figure 6c).

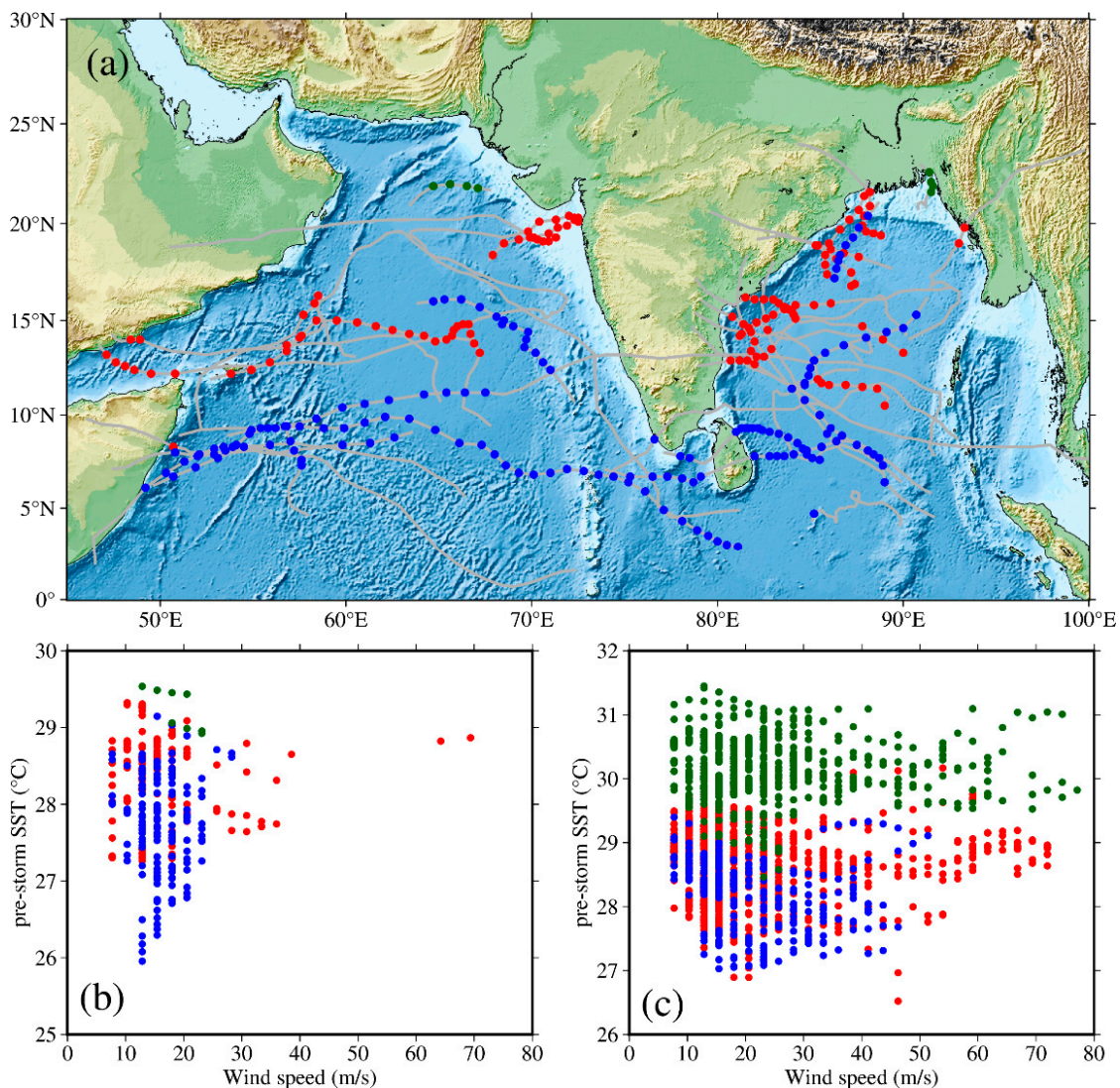


**Figure 6.** (a) Tracks of TCs indicating their positions with positive  $\Delta$ SST values. Scatterplots illustrate the relationship between the wind speeds of TCs and the corresponding climatological SSTs for locations with (b) positive  $\Delta$ SST values and (c) other locations. In both scatterplots, colored points are used to indicate the season of occurrence, e.g., red represents autumn, blue represents winter, and green represents other seasons.

To examine the temporal dependence of SST on TCs, the daily  $\delta$ SST values were averaged over a period of 15 days before and after the passage of a TC, incorporating data from all TC locations. This analysis aims to assess the temporal evolution and quantify the magnitude of TC-induced ocean cooling (Figure 7). The results reveal a distinct pattern in the temporal evolution of SST. The average  $\delta$ SST begins to decrease gradually four days prior to the TC's arrival. This early decline can be attributed to the TC's wide coverage, affecting the SST at a location before its center reaches that point. The cooling process continues to intensify persistently until two days after the TC's passage, reaching its peak cooling extent at approximately  $-0.46 \pm 0.01$  °C. Subsequently, the  $\delta$ SST gradually relaxes, indicating a recovery phase. However, even after 15 days from the TC's passage, the SST remains lower than the corresponding climatological values. Specifically, the average  $\delta$ SST values before and after the TC are  $+0.08$  °C and  $-0.38$  °C, respectively, resulting an overall  $\Delta$ SST of  $-0.46$  °C.

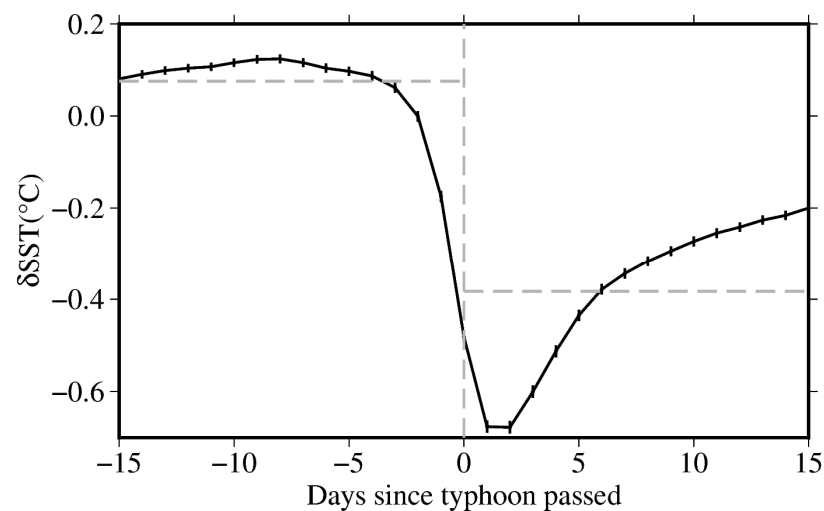


**Figure 7.** Time series of averaged  $\delta$ SST and standard errors (vertical bars) before and after the passage of a TC.

### 3.3. Factors Determining TC-Induced Cooling

The intensity and translation speed of TCs play significant roles in determining the magnitude of TC-induced SST response. In fact, there is a clear relationship between the wind speed of TCs and the corresponding  $\Delta$ SST (Figure 8a). The correlation coefficient between these variables is highly significant, measuring  $-0.96$ . For weak TCs, the average  $\Delta$ SST is only around  $-0.3$  °C, whereas strong TCs result in an average  $\Delta$ SST exceeding  $-0.70$  °C. The TC-induced cooling exhibits a monotonically increasing trend with wind intensity, and a linear regression analysis is employed to quantify the relationship between the averaged  $\Delta$ SST and wind speed. Furthermore, there is a strong correlation between the translation speed of TCs and the averaged  $\Delta$ SST (Figure 8b). The correlation coefficient between these factors is  $0.87$ . This finding aligns with previous studies, suggesting that slow-moving TCs induce more substantial SST cooling in the NIO. Interestingly, when TCs have a translation speed of less than 4 m/s, there is less variation in  $\Delta$ SST, implying that the translation speed has a relatively smaller impact on the magnitude of cooling in these cases.

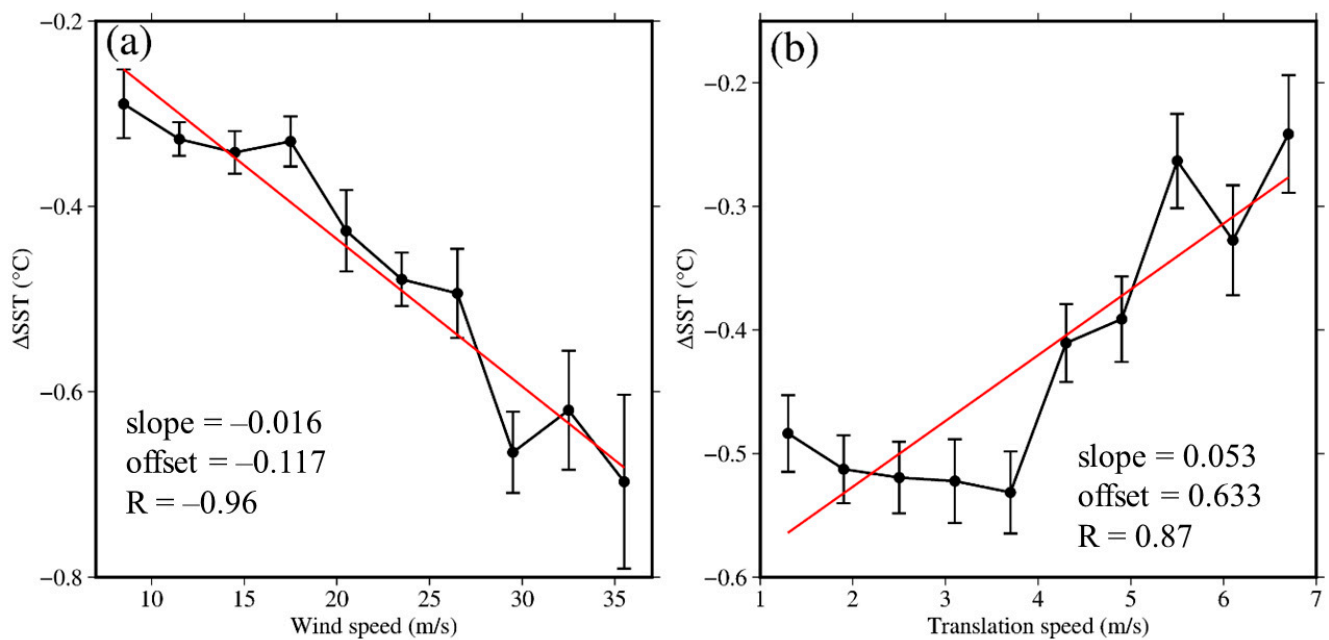


**Figure 8.** Bins of (a) wind speed and (b) translation speed of TCs and the corresponding average and standard error (vertical bars) of  $\Delta$ SST. Linear regressions (red lines) were performed to determine the relationship between the features of TCs and bin-averaged  $\Delta$ SST. The offset and slope of the regression line are labeled in each panel.

#### 4. Discussion

In this study, satellite observations were utilized with a composite method to quantify the SST changes induced by TCs in NIO over an 18-year period. The findings generally align with previous studies [5,17], indicating that SST cooling is a common occurrence following most TCs in the NIO. The observed changes, as discussed in Section 3.2, are consistent with previous research. In particular, the TC-induced SST cooling was a prominent feature throughout the NIO for the majority of TCs (Figure 5). The average reduction in SST was estimated to be 0.8 °C (Figure 7). The time series of TC-induced SST (Figure 7) presented a similar pattern to previous studies (e.g., [49–51]), although the calculated  $\Delta$ SST values differed. For example, previous studies reported cooling values of up to 3 °C, which were generally higher than those obtained in this study. These discrepancies can be attributed to various factors, including the dataset used, the observation periods, and the spatial distance of the observations. One factor contributing to the differences in cooling estimates is the timing of the observations. The largest  $\delta$ SST values were observed within two days after the TCs' passage (Figure 7). However, ship measurements during this period were often hindered by harsh weather conditions, resulting in smaller reported values. Ship observations tended to capture SST rebound as the cruises were typically conducted during this phase [28]. Satellite observations, on the other hand, may be affected by cloud coverage during TC passage [51]. To mitigate this impact, a substantial number of TC locations and merged satellite datasets were employed in this study to filter out the influence of clouds. In situ measurements, such as buoys and moorings, are less susceptible to weather conditions. However, TC tracks rarely pass directly over these instruments [52]. Additionally, Kuttippurath et al. [50] employed a narrower along-track strip (1° width) to assess TC-induced changes, resulting in larger cooling values compared to the results obtained in this study. This discrepancy could be attributed to the fact that SST cooling gradually declined from the center of the TC to its surroundings [34]. Focusing on the small region around the TC centers would yield higher cooling values. Therefore, a comprehensive analysis encompassing all TCs is necessary to accurately quantify the oceanic responses induced by TCs.

To enhance the understanding of TC-induced oceanic responses in the NIO, a comprehensive evaluation was conducted using 1981 TC locations (Figure 1b). A consistent calculation method was applied to ensure a reliable and objective assessment. In comparison to some studies that primarily focus on post-landfall SST cooling on a single day [53], our analysis considers variations in SST (Figure 5). This method provides a more comprehensive representation of the impact of TCs on SST and can be applied to capture the full extent of changes induced by TCs in any ocean basin. To quantify the impact of a TC, it is common practice to use ocean conditions preceding the TC as a reference. Previous studies have shown variations in the initiation of SST changes, ranging from one week before the TC to after the TC [54,55]. However, our results demonstrate that SST remains relatively stable until approximately 4 days before the passage of the TC (Figure 7). Therefore, when selecting a reference value, it is advisable to consider a timeframe of approximately one week in advance of the TC passage to capture the baseline oceanic conditions. This allows for a more accurate assessment of the changes induced by the TC.

The passage of a TC may occur over a relatively short period, but the strong wind forcing associated with the TC has a direct impact on the local sea surface (Figure 3). This leads to significant cooling of SST (Figure 5). The cold SST patches induced by TCs can persist for a much longer duration and may not fully recover to the climatological values even after 15 days (Figure 7). The recovery period of SST following TC-induced cooling can vary. For instance, Vincent et al. [56], in a global-scale evaluation of temperature response to TCs, found that surface cooling is typically restored within 30 days. However, Price et al. [57] observed that the  $\Delta$ SST induced by TC Fabian returned to its initial state within a period of 5 days. These variations in recovery time may be influenced by regional and seasonal ocean conditions, such as the specific time and location of TC occurrence [58]. It is worth noting that the recovery time can be affected by the presence or absence of a thermocline. Jansen et al. [59] discovered that SSTs in regions where the thermocline has been disrupted may persist at intersessional time scales. This persistence can contribute to the recovery of ocean surface cooling induced by TCs.

TC-induced warming accounted for approximately 14% of the total locations, which aligns with findings reported by other researchers [44,60,61]. The study further identified that warming events typically occurred in the latitude range of 8°–15° N (Figure 6). This pattern of increasing TC-induced  $\Delta$ SST can be attributed to two mechanisms. Firstly, the advection of warm water from lower latitudes towards higher latitudes plays a role in generating positive  $\Delta$ SST values [62]. This phenomenon is more prevalent during winter due to the greater meridional SST difference, making it easier for TC-induced horizontal advection to result in warming events [60]. During winter, TCs with positive  $\Delta$ SST values were found to have a deeper mixed layer compared to those with negative  $\Delta$ SST values (Figure 9). However, the mixing induced by these TCs does not always penetrate beyond the pre-storm mixing depth. Additionally, the advected warm water replaces the previously lower SST (Figure 2a). Secondly, there is a subsurface warm layer at the depth of 20–60 m in the Bay of Bengal, primarily due to freshwater input from river discharge and monsoon rain [61]. The shallow topography of the Bay of Bengal facilitates the formation of subsurface warm water through coastal riverine discharge, which has higher density. When TC-induced mixing occurs, the subsurface warm layer is mixed up, resulting in an increase in SST [20]. Previous studies using in situ measurement and numerical models have extensively investigated this feature and have shown that when mixing introduces subsurface warm water to the surface, there is no cold wake phenomenon [61]. The existence of the pre-storm subsurface warm layer has been confirmed through mooring observations during the passage of TC Phailin [63].

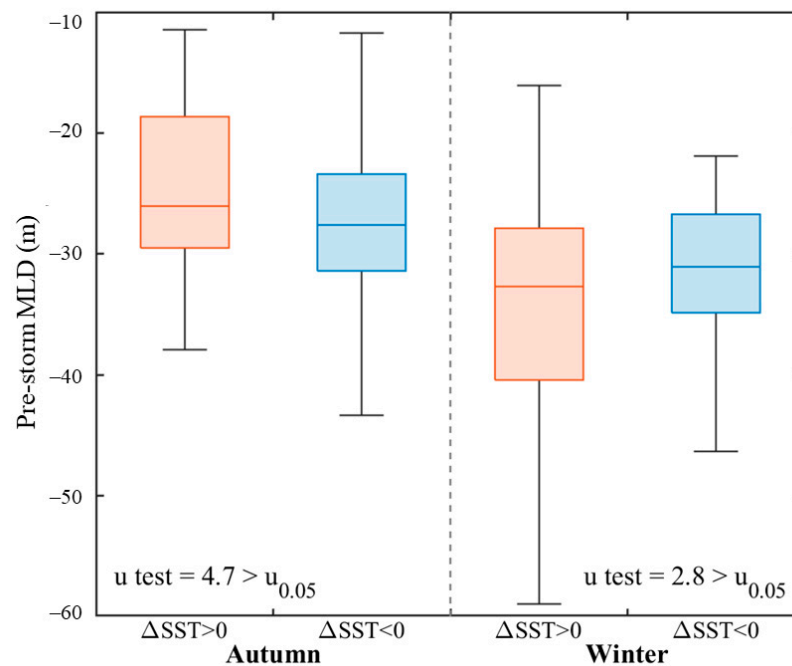


**Figure 9.** Difference in pre-storm MLD between TC locations with (red box) positive and (blue box) negative  $\Delta$ SST values for both (left) autumn and (right) winter seasons. The boxes represent the interquartile range (IQR), with the horizontal line inside each box indicating the median. The whiskers extend from the quartiles to another 1.5 times the IQR, unless they exceed the maximum or minimum values. The difference between the two categories for each season is significant at the 95% confidence level.

All introductions of SST warming by all TCs are objectively analyzed in a comprehensive manner to highlight their spatial and temporal patterns. The majority of TC centers with positive  $\Delta$ SST values were observed during autumn and exhibited wind speeds ranging from 10 to 25 m/s. By employing the methodologies described in Rumyantseva et al. [64] and Jiang et al. [65], the corresponding mixing depth induced by these TCs was estimated to be approximately 30 m. During autumn, TCs were generally weaker in intensity and passed over shallower MLDs (Figure 9). As a result, instead of breaking through the thermal inversion layer, these TCs lifted subsurface warm layers to the surface. This process triggered SST warming during the passage of the TCs [61]. It is worth noting that this phenomenon of abnormal warming is not confined to the Bay of Bengal alone but also in the Arabian Sea. The study sheds light on the need for further investigations to explore the underlying dynamics driving TC-induced warming in the NIO.

In this study, a linear regression analysis was employed to depict the dependence of TC-induced changes on the features of TCs (Figure 8a). However, it should be noted that the actual relationship between these factors is nonlinear [53]. The regression analysis was helpful in assessing the dependence, as the TC-induced responses exhibited a monotonically increasing trend with TC intensity and a decreasing trend with translation speed. The regression coefficients obtained in this study were larger than those reported in the eastern North Pacific and South China Sea [34], indicating that the SST response in the NIO is more sensitive to TC features. Similar results to Figure 8b were also presented by Pothapakula et al. [66], although their study reported lower correlation coefficients between translation speed and  $\Delta$ SST compared to the results of this study. The difference in correlation could be attributed to the use of different SST datasets. It is worth noting that TC-induced flow can cause horizontal convergence near the coast, leading to downwelling that thickens the upper mixed layer and reduces the downward heat flux in the subsurface layer. This process results in warming of the upper-layer ocean [67,68]. Mei and Pasquero [69] found that SST cooling decreased by 220% as TC translation speed increased, which is consistent

with the findings of this study (Figure 8b). The utilization of a consistent dataset for capturing oceanic features in this study enables a quantitative delineation of TC-induced changes. This approach provides a means to assess the impact of TCs and offers valuable insights into the relationships between TC features and their associated changes in SST.

## 5. Conclusions

This study primarily focuses on the distribution of TCs in the NIO and employs a composite method to analyze the SST response to TCs. The study identifies two main variables, namely wind speed and translational speed, as influential factors in determining the variation in SST. The results provide a quantitative depiction of the overall changes and characteristics of the SST response to TCs. The study finds that strong winds and slow-moving TCs have a significant impact on SST. Moreover, the study highlights the large ratio of TC-induced warming in the area, which can be attributed to the underlying mechanisms and upper ocean structure. These conditions can sustain and intensify the TCs over time [18]. Understanding these mechanisms and the characteristics of temperature response to TCs is crucial for predicting the evolution of TCs.

Moving forward, it is recommended that future studies delve into individual basins in more detail. This would allow for a better understanding of the specific characteristics of temperature response to TCs, which can further enhance predictions of TC evolution. By focusing on individual basins, researchers can uncover basin-specific dynamics and factors that influence the temperature response, leading to more accurate forecasts and improved understanding of TC behavior in different regions.

**Author Contributions:** Visualization, investigation, data curation, writing, J.Y. and S.T.; funding, conceptualization, Y.W.; review of the manuscript, H.L. All authors have read and agreed to the published version of the manuscript.

**Funding:** The study was funded by the Strategic Priority Research Program, Chinese Academy of Sciences, China (grant No. XDB42000000) and Fundamental Research Fund of Second Institute of Oceanography, MNR (grant No. QNYC2202).

**Institutional Review Board Statement:** Not applicable.

**Informed Consent Statement:** Not applicable.

**Data Availability Statement:** We are grateful for the tropical cyclone dataset from the Joint Typhoon Warning Center (JTWC) (<http://www.metoc.navy.mil/jtwc/jtwc.html>), assessed on 1 April 2023, and the merged SST datasets from the Remote Sensing System (<http://www.remss.com>), assessed on 1 April 2023.

**Acknowledgments:** We are very thankful to the Remote Sensing System and the Joint Typhoon Warning Center (JTWC) for sharing their datasets. We are very thankful to the Generic Mapping Tools 6 to generate all figures.

**Conflicts of Interest:** The authors declare no conflict of interest.

## References

1. Emanuel, K. Increasing destructiveness of tropical cyclones over the past 30 years. *Nature* **2005**, *436*, 686–688. [[CrossRef](#)] [[PubMed](#)]
2. Kotal, S.D.; Bhowmik, P.K.; Kundu, A.K. A Statistical Cyclone Intensity Prediction (SCIP) model for the Bay of Bengal. *J. Earth Syst. Sci.* **2008**, *117*, 157–168. [[CrossRef](#)]
3. Guan, S.; Zhao, W.; Sun, L.; Zhou, C.; Hou, Y. Tropical cyclone-induced sea surface cooling over the Yellow Sea and Bohai Sea in the 2019 Pacific typhoon season. *J. Mar. Syst.* **2021**, *217*, 103509. [[CrossRef](#)]
4. Li, Z.; Li, T.; Yu, W.; Li, K.; Liu, Y. What controls the interannual variation of tropical cyclone genesis frequency over Bay of Bengal in the post-monsoon peak season? *Atmos. Sci. Lett.* **2016**, *17*, 148–154. [[CrossRef](#)]
5. Vinodhkumar, B.; Busireddy, N.; Ankur, K.; Nadimpalli, R.; Osuri, K.K. On Occurrence of Rapid Intensification and Rainfall changes in Tropical Cyclones over the North Indian Ocean. *Int. J. Climatol.* **2021**, *42*, 714–726. [[CrossRef](#)]
6. Krishnamohan, K.S.; Mohanakumar, K.; Joseph, P. V The influence of madden–Julian oscillation in the genesis of north Indian ocean tropical cyclones. *Theor. Appl. Climatol.* **2012**, *109*, 271–282. [[CrossRef](#)]
7. Kuttippurath, J.; Sunanda, N.; Martin, M.V.; Chakraborty, K. Tropical storms trigger phytoplankton blooms in the deserts of north Indian ocean. *Environ. Sci. Atmos.* **2022**, *4*, 404–415. [[CrossRef](#)]

8. Lin, S.; Wang, Y.; Zhang, W.-Z.; Ni, Q.-B.; Chai, F. Tropical cyclones related wind power on oceanic near-inertial oscillations. *Geophys. Res. Lett.* **2023**, *50*, e2023GL105056. [[CrossRef](#)]
9. Uddin, M.J.; Nasrin, Z.M.; Li, Y. Effects of vertical wind shear and storm motion on tropical cyclone rainfall asymmetries over the north Indian ocean. *Dyn. Atmos. Ocean.* **2021**, *93*, 101196. [[CrossRef](#)]
10. Dasol, K.; Ho, C.H.; Park, D.; Chan, J.; Jung, Y. The relationship between tropical cyclone rainfall area and environmental conditions over the subtropical oceans. *J. Clim.* **2018**, *31*, 4605–4616.
11. Woodruff, J.D.; Irish, J.L.; Camargo, S.J. Coastal flooding by tropical cyclones and sea-level rise. *Nature* **2013**, *504*, 44–52. [[CrossRef](#)] [[PubMed](#)]
12. Lin, I.I.; Chen, C.H.; Pun, I.F.; Liu, W.T.; Wu, C.C. Warm Ocean anomaly, air sea fluxes, and the rapid intensification of tropical cyclone Nargis (2008). *Geophys. Res. Lett.* **2009**, *36*, L03817. [[CrossRef](#)]
13. Roxy, M.K.; Dasgupta, P.; McPhaden, M.J.; Suematsu, T.; Kim, D. Twofold expansion of the Indo-Pacific warm pool warps the MJO life cycle. *Nature* **2019**, *575*, 647–651. [[CrossRef](#)] [[PubMed](#)]
14. Wang, S.; Toumi, R. Recent migration of tropical cyclones toward coasts. *Science* **2021**, *371*, 514–517. [[CrossRef](#)]
15. Andreas, E.L.; Persson, P.O.G.; Hare, J.E. A bulk turbulent air-sea flux algorithm for high-wind, spray conditions. *J. Phys. Oceanogr.* **2008**, *38*, 1581–1596. [[CrossRef](#)]
16. Bhalachandran, S.; Nadimpalli, R.; Osuri, K.K.; Marks, F.D.; Gopalakrishnan, S.; Subramanian, S.; Mohanty, U.C.; Niyogi, D. On the processes influencing rapid intensity changes of tropical cyclones over the Bay of Bengal. *Sci. Rep.* **2019**, *9*, 3882. [[CrossRef](#)] [[PubMed](#)]
17. Deshpande, M.; Singh, V.; Ganadhi, M.K.; Roxy, M.K.; Emmanuel, R.; Kumar, U. Changing status of tropical cyclones over the north Indian Ocean. *Clim. Dyn.* **2021**, *57*, 3545–3567. [[CrossRef](#)]
18. Singh, V.K.; Roxy, M.K. A review of ocean-atmosphere interactions during tropical cyclones in the North Indian Ocean. *Ear-Sci. Rev.* **2022**, *226*, 103967. [[CrossRef](#)]
19. Hart, R.E.; Maue, R.N.; Watson, M.C. Estimating local memory of tropical cyclones through MPI anomaly evolution. *Mon. Weather Rev.* **2007**, *135*, 3990–4005. [[CrossRef](#)]
20. Sengupta, D.; Goddalahundi, B.R.; Anitha, D.S. Cyclone-induced mixing does not cool SST in the post-monsoon north Bay of Bengal. *Atmos. Sci. Lett.* **2008**, *9*, 1–6. [[CrossRef](#)]
21. Lloyd, I.D.; Vecchi, G.A. Observational evidence for oceanic controls on hurricane intensity. *J. Clim.* **2010**, *24*, 1138–1153. [[CrossRef](#)]
22. Neetu, S.; Lengaigne, M.; Vincent, E.M.; Vialard, J.; Durand, F.; Madec, G.; Samson, G.; Kumar, M.R.R. Influence of oceanic stratification on tropical cyclones-induced surface cooling in the Bay of Bengal. *J. Geophys. Res.* **2012**, *117*, C12020. [[CrossRef](#)]
23. Chowdhury, R.R.; Prasanna, K.S.; Narvekar, J.; Chakraborty, A. Back-to-Back Occurrence of Tropical Cyclones in the Arabian Sea During October–November 2015: Causes and Responses. *J. Geophys. Res.-Ocean.* **2020**, *125*, e2019JC015836. [[CrossRef](#)]
24. Sanabia, E.R.; Barrett, B.S.; Black, P.G.; Chen, S.; Cummings, J.A. Real-time upper-ocean temperature observations from aircraft during operational hurricane reconnaissance missions: AXBT demonstration project year one results. *Weather Forecast.* **2012**, *28*, 1404–1422. [[CrossRef](#)]
25. Kim, H.S.; Lozano, C.; Tallapragada, V.; Iredell, D.; Sheinin, D.; Tolman, H.L.; Gerald, V.M.; Sims, J. Performance of ocean simulations in the coupled HWRF–HYCOM model. *J. Atmos. Ocean. Technol.* **2013**, *31*, 545–559. [[CrossRef](#)]
26. Yablonsky, R.M.; Ginis, I. Impact of a warm ocean eddy’s circulation on hurricane-induced sea surface cooling with implications for hurricane intensity. *Mon. Weather Rev.* **2013**, *141*, 997–1021. [[CrossRef](#)]
27. Girishkumar, M.S.; Suprit, K.; Chiranjivi, J.; Bhaskar, T.U.; Ravichandran, M.; Shesu, R.V.; Rao, E.P.R. Observed oceanic response to tropical cyclone Jal from a moored buoy in the south-western Bay of Bengal. *Ocean Dyn.* **2014**, *64*, 325–335. [[CrossRef](#)]
28. Yu, L.; McPhaden, M.J. Ocean preconditioning of Cyclone Nargis in the Bay of Bengal: Interaction between Rossby waves, Surface Fresh Waters, and Sea Surface Temperatures. *J. Phys. Oceanogr.* **2019**, *41*, 1741–1755. [[CrossRef](#)]
29. Lin, I.; Wu, C.; Pun, I.; Ko, D. Upper-ocean thermal structure and the western north Pacific category 5 typhoons. part I: Ocean features and the category 5 typhoons’ intensification. *Mon. Weather Rev.* **2008**, *136*, 3288–3306. [[CrossRef](#)]
30. Sandery, P.A.; Brassington, G.B.; Craig, A.; Pugh, T. Impacts of ocean–atmosphere coupling on tropical cyclone intensity changes and ocean prediction in the Australian region. *Mon. Weather Rev.* **2010**, *138*, 2074–2091. [[CrossRef](#)]
31. Blazhko, V.N.; Chefranov, S.G. Dissipative-centrifugal instability of tropical disturbances and the initial stage of tropical-cyclone development. *Izv. Atmos. Ocean. Phys.* **2005**, *41*, 537–544.
32. Hoarau, K.; Bernard, J.; Chalonge, L. Intense tropical cyclone activities in the northern Indian ocean. *Int. J. Climatol.* **2012**, *32*, 1935–1945. [[CrossRef](#)]
33. Albert, J.; Bhaskaran, P.K. Ocean heat content and its role in tropical cyclogenesis for the Bay of Bengal basin. *Clim. Dyn.* **2020**, *55*, 3343–3362. [[CrossRef](#)]
34. Wang, Y. Composite of typhoon induced sea surface temperature and chlorophyll-a responses in the South China Sea. *J. Geophys. Res. Ocean.* **2020**, *125*, e2020JC016243. [[CrossRef](#)]
35. D’Asaro, E.; Black, P.; Centurioni, L.; Harr, P.; Jayne, S.; Lin, I.I.; Lee, C.; Morzel, J.; Mrvaljevic, R.; Niiler, P.; et al. Typhoon-ocean interaction in the western north Pacific: Part 1. *Oceanography* **2011**, *24*, 24–31. [[CrossRef](#)]
36. D’Asaro, E.; Black, P.; Centurioni, L.; Chang, Y.; Chen, S.; Foster, R.C.; Graber, H.C.; Harr, P.; Hormann, V.; Lien, R.-C.; et al. Impact of typhoons on the ocean in the Pacific. *Bull. Am. Meteorol. Soc.* **2014**, *95*, 1405–1418. [[CrossRef](#)]
37. Zedler, S.E. Simulations of the ocean response to a hurricane: Nonlinear processes. *J. Phys. Oceanogr.* **2009**, *39*, 2618–2634. [[CrossRef](#)]

38. Ali, S.A.; Mao, Z.; Wu, J.; Chen, X.; Zhu, Q.; Huang, H.; Gong, F.; Wang, T. Satellite Evidence of Upper Ocean Responses to Cyclone Nilofar. *Atmosphere-Ocean* **2020**, *58*, 13–24. [[CrossRef](#)]
39. Fu, D.; Luan, H.; Pan, D.; Zhang, Y.; Wang, L.A.; Liu, D.; Ding, Y.; Li, X. Impact of two typhoons on the marine environment in the Yellow Sea and East China Sea. *Chin J. Oceanol. Limnol.* **2014**, *34*, 871–884. [[CrossRef](#)]
40. Li, Z.; Yu, W.; Li, T.; Murty, V.S.N.; Tangang, F. Bimodal Character of Cyclone Climatology in the Bay of Bengal Modulated by Monsoon Seasonal Cycle. *J. Clim.* **2013**, *26*, 1033–1046. [[CrossRef](#)]
41. Busireddy, N.K.R.; Ankur, K.; Osuri, K.K.; Sivareddy, S.; Niyogi, D. The response of ocean parameters to tropical cyclones in the Bay of Bengal. *Q. J. R. Meteorol. Soc.* **2019**, *145*, 3320–3332. [[CrossRef](#)]
42. Rajasree, V.; Kesarkar, A.P.; Bhate, J.N.; Umakanth, U.; Singh, V.; Varma, T.H. Appraisal of recent theories to understand cyclogenesis pathways of tropical cyclone Madi (2013). *J. Geophys. Res. Atmos.* **2016**, *121*, 8949–8982. [[CrossRef](#)]
43. Osuri, K.K.; Nadimpalli, R.; Mohanty, U.C.; Niyogi, D. Prediction of rapid intensification of tropical cyclone Phailin over the Bay of Bengal using the HWRF modelling system. *Q. J. R. Meteorol. Soc.* **2016**, *143*, 678–690. [[CrossRef](#)]
44. Chacko, N. Effect of Cyclone Thane in the Bay of Bengal Explored Using Moored Buoy Observations and Multi-platform Satellite Data. *J. Indian Soc. Remote Sens.* **2018**, *46*, 821–828. [[CrossRef](#)]
45. Mohapatra, M.; Bandyopadhyay, B.K.; Tyagi, A. Best track parameters of tropical cyclones over the North Indian Ocean: A review. *Nat. Hazards* **2012**, *63*, 1285–1317. [[CrossRef](#)]
46. Lu, S.; Liu, Z.; Li, H.; Li, Z.; Wu, X.; Sun, C.; Xu, J. Manual of Global Ocean Argo Gridded Data Set (BOA\_Argo) (Version 2019). 2020, p. 14. Available online: [http://argo.ucsd.edu/wp-content/uploads/sites/361/2020/07/User\\_Manual\\_BOA\\_Argo-2020.pdf](http://argo.ucsd.edu/wp-content/uploads/sites/361/2020/07/User_Manual_BOA_Argo-2020.pdf) (accessed on 1 June 2023).
47. Duan, W.; Yuan, J.; Duan, X.; Feng, D. Seasonal Variation of Tropical Cyclone Genesis and the Related Large-Scale Environments: Comparison between the Bay of Bengal and Arabian Sea Sub-Basins. *Atmosphere* **2021**, *12*, 1593. [[CrossRef](#)]
48. Wang, Y.; Ma, W.; Zhou, F.; Chai, F. Frontal variability and its impact on chlorophyll in the Arabian Sea. *J. Mar. Syst.* **2021**, *218*, 103545. [[CrossRef](#)]
49. Dare, R.A.; McBride, J.L. Sea surface temperature response to tropical cyclones. *Mon. Weather Rev.* **2011**, *139*, 3798–3808. [[CrossRef](#)]
50. Kuttippurath, J.; Akhila, R.S.; Martin, M.V.; Girishkumar, M.S.; Mohapatra, M.; Sarojini, B.B.; Mogensen, K.; Sunanda, N.; Chakraborty, A. Tropical cyclone-induced cold wakes in the northeast Indian ocean. *Environ. Sci. Atmos.* **2022**, *2*, 404. [[CrossRef](#)]
51. Chen, C.; Tang, D. Eddy-feature phytoplankton bloom induced by a tropical cyclone in the South China Sea. *Int. J. Remote Sens.* **2012**, *33*, 7444–7457. [[CrossRef](#)]
52. Zhang, H.; Wu, R.; Chen, D.; Liu, X.; He, H.; Tang, Y.; Ke, D.; Shen, Z.; Li, J.; Xie, J.; et al. Net modulation of upper ocean thermal structure by Typhoon Kalmaegi (2014). *J. Geophys. Res. Ocean.* **2014**, *122*, 7154–7171. [[CrossRef](#)]
53. Lengaigne, M.; Neetu, S.; Samson, G.; Vialard, J.; Krishnamohan, K.S.; Masson, S.; Jullien, S.; Suresh, I.; Menkes, C.E. Influence of air–sea coupling on Indian ocean tropical cyclones. *Clim. Dyn.* **2018**, *52*, 577–598. [[CrossRef](#)]
54. Vidya, P.J.; Das, S.; Mani, M.R. Contrasting Chl-a responses to the tropical cyclone’s thane and Phailin in the Bay of Bengal. *J. Mar. Sys.* **2017**, *165*, 103–114.
55. Chinta, V.; Deo, A.A. Study of upper ocean parameters during passage of tropical cyclones over Indian seas. *Int. J. Remote Sens.* **2019**, *40*, 4683–4723.
56. Vincent, E.M.; Lengaigne, M.; Madec, G.; Vialard, J.; Samson, G.; Jourdain, N.C.; Menkes, C.E.; Jullien, S. Processes setting the characteristics of sea surface cooling induced by tropical cyclones. *J. Geophys. Res.* **2012**, *117*, C02020. [[CrossRef](#)]
57. Price, J.F.; Morzel, J.; Niiler, P.P. Warming of sst in the cool wake of a moving hurricane. *J. Geophys. Res.* **2008**, *113*, C07010. [[CrossRef](#)]
58. Cheng, L.; Zhu, J.; Sriviver, R.L. Global representation of tropical cyclone-induced short-term ocean thermal changes using argo data. *Ocean Sci.* **2015**, *11*, 719–741. [[CrossRef](#)]
59. Jansen, M.F.; Ferrari, R.; Mooring, T.A. Seasonal versus permanent thermocline warming by tropical cyclones. *Geophys. Res. Lett.* **2010**, *37*, 202–217. [[CrossRef](#)]
60. Girishkumar, M.S.; Ravichandran, M.; McPhaden, M.J. Temperature inversions and their influence on the mixed layer heat budget during the winters of 2006–2007 and 2007–2008 in the Bay of Bengal. *J. Geophys. Res. Ocean.* **2013**, *118*, 2426–2437. [[CrossRef](#)]
61. Jarugula, S.L.; McPhaden, M.J. Ocean mixed layer response to two post-monsoon cyclones in the Bay of Bengal in 2018. *J. Geophys. Res. Ocean.* **2022**, *127*, e2022JC018874. [[CrossRef](#)]
62. Jian, L.; Lei, Y.; Shu, Y.; Wang, D. Temperature Inversion in the Bay of Bengal Prior to the Summer Monsoon Onsets in 2010 and 2011. *Atmos. Oceanic Sci. Lett.* **2012**, *5*, 290–294. [[CrossRef](#)]
63. Chaudhuri, D.; Sengupta, D.; D’Asaro, E.; Venkatesan, R.; Ravichandran, M. Response of the Salinity-Stratified Bay of Bengal to Cyclone Phailin. *J. Phys. Oceanogr.* **2019**, *49*, 121–1140. [[CrossRef](#)]
64. Rummyantseva, A.; Henson, S.; Martin, A.; Thompson, D.F.; Damerell, G.M.; Kaiser, J.; Heywood, K.J. Phytoplankton spring bloom initiation: The impact of atmospheric forcing and light in the temperate North Atlantic Ocean. *Prog. Oceanogr.* **2019**, *178*, 102202. [[CrossRef](#)]
65. Jiang, Y.; Wang, Y.; Tian, X.; Lin, S.; Chen, S.; Yu, J.; Chai, F. Upper Ocean Structure Determines the Contrasting Typhoon-Induced Chlorophyll-a Responses in the Northwest Pacific. *Geophys. Res. Lett.* **2023**, *50*, e2023GL102930. [[CrossRef](#)]
66. Pothapakula, P.K.; Osuri, K.K.; Pattanayak, S.; Mohanty, U.C.; Prasad, S.K. Observational perspective of SST changes during life cycle of tropical cyclones over Bay of Bengal. *Nat. Hazards* **2016**, *88*, 1769–1787. [[CrossRef](#)]

67. Tsai, Y.; Chern, C.S.; Wang, J. Numerical study of typhoon-induced ocean thermal content variations on the northern shelf of the South China Sea. *Cont. Shelf Res.* **2012**, *42*, 64–77. [[CrossRef](#)]
68. Kuo, Y.C.; Lee, M.A.; Chern, C.S. Typhoon-induced Ocean responses off the southwest coast of Taiwan. *Ocean Dyn.* **2014**, *64*, 1569–1581. [[CrossRef](#)]
69. Mei, W.; Pasquero, C. Spatial and temporal characterization of sea surface temperature response to tropical cyclones. *J. Clim.* **2013**, *26*, 3745–3766. [[CrossRef](#)]

**Disclaimer/Publisher’s Note:** The statements, opinions and data contained in all publications are solely those of the individual author(s) and contributor(s) and not of MDPI and/or the editor(s). MDPI and/or the editor(s) disclaim responsibility for any injury to people or property resulting from any ideas, methods, instructions or products referred to in the content.